Structural and electronic inhomogeneity of superconducting Nb-doped Bi₂Se₃

Simone M. Kevy,[1] Henriette E. Lund ◉,[2] Laura Wollesen ◉,[1] Kirstine J. Dalgaard,[1] Yu-Te Hsu,[3] Steffen Wiedmann ◉,[3]
Marco Bianchi,[2] Ann Julie Utne Holt,[2] Davide Curcio,[2] Deepnarayan Biswas,[2] Alfred J. H. Jones ◉,[2] Klara Volckaert,[2]
Cephise Cacho ◉,[4] Pavel Dudin ◉,[4] Philip Hofmann ◉,[2] and Martin Bremholm ◉[1,*]

[1]*Department of Chemistry, Interdisciplinary Nanoscience Center (iNANO), Aarhus University, 8000 Aarhus C, Denmark*
[2]*Department of Physics and Astronomy, Interdisciplinary Nanoscience Center (iNANO), Aarhus University, 8000 Aarhus C, Denmark*
[3]*High Field Magnet Laboratory and Institute for Molecules and Materials, Radboud University, 6525 ED Nijmegen, Netherlands*
[4]*Diamond Light Source, Harwell Campus, Didcot OX11 0DE, United Kingdom*

The crystal structure, electronic structure, and transport properties of crystals with the nominal composition $Nb_{0.25}Bi_2Se_3$ are investigated. X-ray diffraction reveals that the as-grown crystals display phase segregation and contain major contributions of BiSe and the superconducting misfit layer compound $(BiSe)_{1.1}NbSe_2$. The inhomogeneous character of the samples is also reflected in the electronic structure and transport properties of different single crystals. Angle-resolved photoemission spectroscopy (ARPES) reveals an electronic structure that resembles poor-quality Bi_2Se_3 with an ill-defined topological surface state. High-quality topological surface states are instead observed when using a highly focused beam size, i.e., nanoARPES. While the superconducting transition temperature is found to vary between 2.5 and 3.5 K, the majority of the bulk single crystals does not exhibit a zero-resistance state suggesting filamentary superconductivity in the materials. Susceptibility measurements of the system together with the temperature dependence of the coherence length extracted from the upper critical field are consistent with conventional BCS superconductivity of a type II superconductor.

I. INTRODUCTION

The interpretation of crystalline band structure phenomena in terms of topology and their connection to concepts of high-energy physics have recently led to a deeper understanding of electronic structure and transport properties, as well as to the discovery of novel surface electronic states in many materials [1–4]. The concept of a topological insulator, a material in which the topological character of the gapped bulk band structure forces the emergence of metallic surface states, could even be extended to define topological superconductors, in which the role of the insulating gap is assumed by the superconducting gap [5]. Topological superconductors are of considerable interest to act as hosts of Majorana quasiparticles which might be applicable in topological quantum computation [6], and a lot of effort is therefore being put into the investigation of candidate materials for topological superconductivity [7].

Intriguingly, it has been suggested that topological insulators of the Bi₂Se₃ family could also be turned into topological superconductors [8]. Bulk doping by Cu [9–13], Sr [14–17], and Nb [18–26] has indeed led to the observation of (not necessarily topological) superconductivity in these materials. The mechanism driving the superconductivity is widely thought to be metal intercalation in the van der Waals gap between the quintuple layers forming the Bi₂Se₃ structure [9]. It has been suggested that the superconducting ground state in the

intercalation compounds could show nematic order [27] and there have been recent experimental indications of this [15,22,28,29]. In the case of Nb-doped Bi₂Se₃, unconventional superconductivity and the presence of a nodal gap in the material has been suggested by several experimental approaches [18,20–22,24,30–32].

The synthesis of Nb-doped Bi₂Se₃ with the desired properties has been found to be not without challenges. It has proven to be difficult to achieve high superconducting shielding fractions and the superconducting properties depend on the details of the synthesis method [12,13,33]. Moreover, the electronic structure of the doped compound can be unexpectedly complex as a result of contributions from other phases [19]. Indeed, Kobayashi *et al.* have recently studied the structural composition of nominal $Nb_xBi_2Se_3$ for $0 < x \leqslant 0.7$ and found small contributions (never more than 5%) of an impurity phase $(BiSe)_{1.1}NbSe_2$ (referred to as BiNbSe₃) and, for higher x, also BiSe [23].

In this paper, we investigate the crystal structure of our samples made from a nominal content of $Nb_{0.25}Bi_2Se_3$ with a special emphasis on the contribution of different crystal phases, and we study the superconducting and electronic properties by magnetic and transport experiments and angle-resolved photoemission spectroscopy (ARPES), including nanoARPES experiments.

We show that the as-grown samples are highly inhomogeneous, containing three crystalline phases and that the phase composition varies strongly across the macroscopic crystal boules. This inhomogeneity is also reflected in the transport properties, implying that studies on the superconductivity of

*bremholm@chem.au.dk

085107-1

the crystals, made from a nominal content of $Nb_{0.25}Bi_2Se_3$, needs to be accompanied by a careful characterization of the phase composition of the particular sample area. Lastly, we present results from an experimental characterization of the superconducting character of the system.

II. EXPERIMENTAL METHODS

Bulk samples with nominal composition of $Nb_{0.25}Bi_2Se_3$ were synthesized through a melt growth method. The pure elements, Bi (99.999%), Se (99.999%), and Nb (99.99%), were mixed in a stoichiometric ratio, evacuated to 10^{-4} mbar, and sealed in a quartz ampoule with a pointy tip. The mixture was then heated at 900–950 °C for 1 day (the ramp rates were 50 °C/h), cooled to 650 °C at a slow rate of 2–6 °C/h, and then quenched in ice water. A complete description of all the samples mentioned in this paper, with their synthesis parameters and basic properties, is given in the Supplemental Material (SM) [34]. The result of a typical growth is a macroscopic crystal boule as shown in Fig. 1(a). For further analysis, each crystal boule was divided into five similar-sized areas following domain boundaries when possible, as schematically indicated in the figure. Seven crystal boules are analyzed in this study. The samples are named as SN-X where a number N (1–7) denotes the entire crystal boule obtained from one quartz tube and the letter X (A–E) a particular area on the crystal boule. SN-A always refers to the part of the sample furthest away from the tip [see Fig. 1(a) and an overview in the SM [34]]. Typically, one crystal boule area was divided into two halves, one crystalline part (for ARPES, or transport measurements), and the other was ground into a fine powder (for magnetic susceptibility and diffraction analyses). Reference samples of Bi_2Se_3, BiSe, and $(BiSe)_{1.1}NbSe_2$ were prepared by mixing elements in stoichiometric ratios (same purity as above), and then evacuated and sealed in quartz ampoules. The mix of BiSe and Bi_2Se_3 was heated to 800 °C (1 day) before being cooled to room temperature: one of 900 °C (held there for 5 days, then room temperature) and one of 950 °C (3 days, then ramped to 800 °C). From 800 °C the slow ramping (6 °C/h) was utilized down to 600 °C, then quenched in ice water. However, heating cycles only generate powdered samples of $(BiSe)_{1.1}NbSe_2$.

The crystal structures of powders from the selected areas were characterized by powder x-ray diffraction (PXRD) on a Rigaku SmartLab diffractometer with Cu $K\alpha_1$ ($\lambda = 1.5406$ Å) radiation and at the P02.1 beamline ($\lambda = 0.207$ Å) at PETRA III, Deutsches Elektronen-Synchrotron (DESY). The magnetotransport experiments were carried out at the High Field Magnet Laboratory (HFML), Nijmegen. The samples used, were typically thin flakes of 100–300 μm thickness with a length and width <3 mm. Wires were attached to the samples with conducting Ag paste. Transport experiments were performed in a vacuum tube equipped with an inner vacuum chamber (IVC). We added sufficient ^{4}He contact gas in the sample space and IVC for measurements at 1.3 K to ensure a good thermal connection. For the temperature sweeps, the IVC was evacuated. Magnetotransport was carried out in either a superconducting or a resistive (Bitter) magnet up to 30 T using standard lock-in detection techniques with an excitation current of 1 mA. The magnetoresistance was measured in a
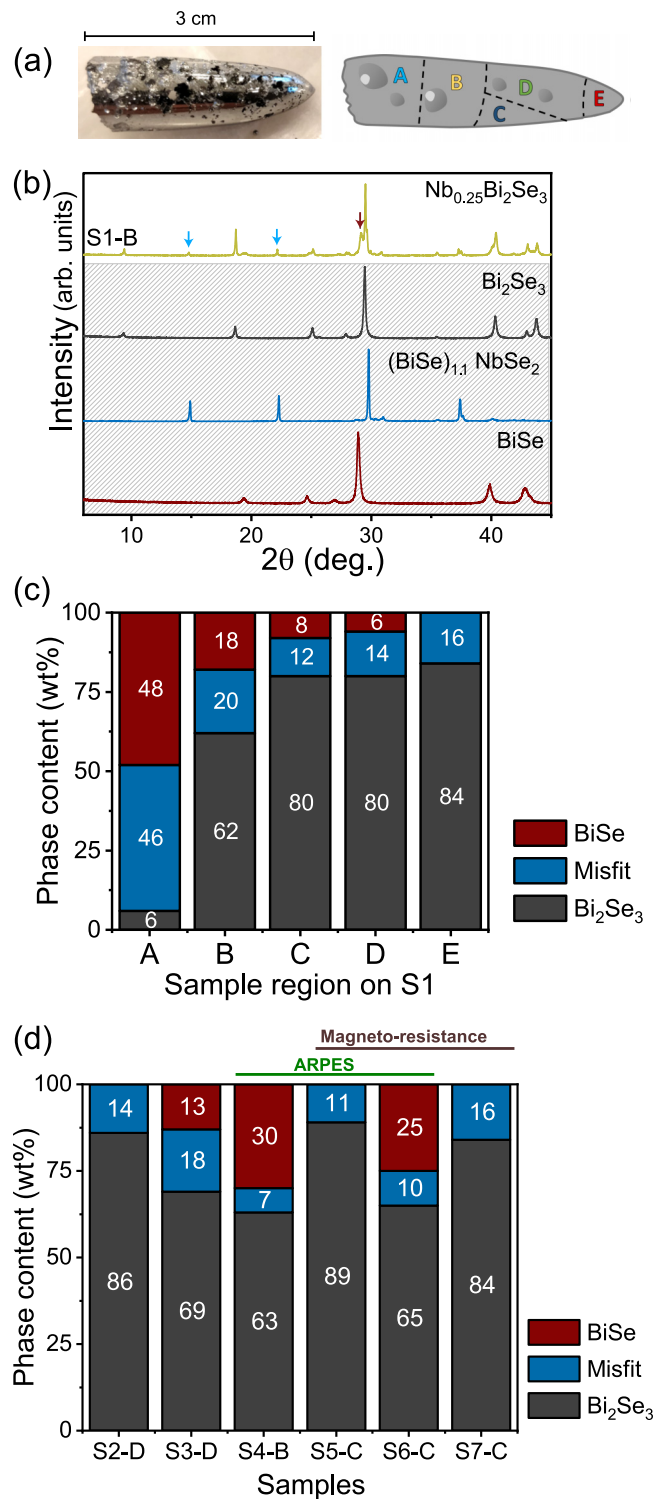

FIG. 1. (a) Picture of the actual sample (S1) with an illustration indicating the approximate location of the areas A–E; the dimension is shown by the scale bar of 3 cm. (b) PXRD pattern of S1-B along with reference samples: Pristine Bi_2Se_3, the misfit layer compound $[(BiSe)_{1.1}NbSe_2]$, and BiSe. Vertical arrows indicate positions of peaks stemming from BiSe and the misfit phase. (c) Phase content (in wt%) of S1 for each of the five areas illustrated in (a). Uncertainties are ±2 for the misfit phase, and ±5 for both BiSe and Bi_2Se_3. (d) Phase content (in wt%) for all the other samples studied in this paper. Lines above indicate performed experiments (ARPES or magnetoresistance) on the displayed samples.

magnetic field $B_\perp$ perpendicular to the flat sample (parallel to the c axis of the Bi_2Se_3 structure) and $B_\parallel$ parallel to the flat sample and perpendicular to the current path. The critical temperature T_C is defined as the temperature corresponding to the maximum of the first derivative of resistance as a function of temperature.

Additional measurements of the temperature dependence of the magnetic susceptibility were performed with a physical property measurement system with the vibrating sample magnetometer option in the range from 1.75 to 10 K [zero-field cooled (ZFC)] in 2 mT. For these, we refer to $T_{C,onset}$, determined as the intersection of tangents of the susceptibility before and after the transition. We refer to both a T_C and $T_{C,onset}$, because no samples show saturation of the magnetic susceptibility to the lowest temperatures measured.

ARPES data were collected at the SGM3 beamline at the ASTRID2 synchrotron radiation facility [35] and at the nanoARPES branch of the I05 beamline at Diamond Light Source [36]. The SGM3 data were collected at a temperature of approximately 30 K, a photon energy of 22 eV, and with a light spot size of approximately $190 \times 90 \ \mu m^2$. The corresponding quantities for I05 were room temperature, 60 eV, and $500(\pm100)$ nm. The small light spot was achieved by using a Fresnel zone plate. Spatially resolved ARPES was then collected by moving the focused light spot across the sample using SmarAct piezo stages and collecting ARPES spectra at each position. Note that during such spatial scans, the emission angle between the sample and electron analyzer remains fixed, such that data from differently oriented domains also result in different cuts in k space. For the ARPES experiments, the energy and angular resolution were better than 15 meV and $0.1°$, respectively. For the nanoARPES experiments, the angular resolution was $0.2°$ and the energy resolution between 80 and 90 meV. The samples were cleaved at room temperature in a pressure better than 7×10^{-8} mbar in both experiments.

III. RESULTS

In the following, we describe the physical properties of the Nb-doped Bi_2Se_3 system with special emphasis on the presence and scale of spatial inhomogeneity and the consequences this has on the electronic and transport properties of the material. A detailed description of all mentioned samples is included in the SM [34], but all are made with a nominal composition of $Nb_{0.25}Bi_2Se_3$.

A. Crystal structure and phase analysis

The crystal structure of all samples was determined by PXRD from powders from the different areas on the crystal boules, such as the one shown in Fig. 1(a). A diffraction pattern taken of S1-B is displayed in Fig. 1(b). When comparing the scan to that of the pure Bi_2Se_3 sample, a number of additional sharp peaks are observed (some are marked by vertical arrows). This indicates that the structure of Nb-doped Bi_2Se_3 is not only that of Bi_2Se_3 with the Nb intercalated in the van der Waals gap but that it contains significant contributions from other crystal phases (a simulation shows that the diffraction pattern corresponding to intercalated Nb in

Bi_2Se_3 would be almost identical to that of pure Bi_2Se_3). The presence of the additional phase was already pointed out in Ref. [23], but we refrain from a direct comparison with our own results as the quantification method was not specified. Instead, we analyze the phase composition in detail here. Qualitatively, the diffraction pattern of the Nb-doped Bi_2Se_3 system can be interpreted as a superposition of diffraction from Bi_2Se_3, the misfit phase $(BiSe)_{1.1}NbSe_2$ [37,38], and bulk BiSe [the powder diffraction patterns of pure reference samples are shown in Fig. 1(b)]. The misfit layer compound consists of alternating layers of Bi-Se square nets (not to be confused with the rhombohedral bulk BiSe) and slabs of [Se-Nb-Se] stacked along the c direction [37,38]. The two types of layers have their unit cells matched perfectly along the b direction but not along the a direction, thus the name "misfit layer compound." The peak widths indicate crystalline domains larger than 100 nm when using the Scherrer equation, possibly much larger since there will be contributions from other broadening effects as well.

The result of a quantitative analysis of the crystal phase content in sample S1 is presented in Fig. 1(c). A series of mixed powders with known amounts of phases was prepared using the reference samples mentioned earlier (further details can be found in the SM [34]). This analysis shows that significant amounts of the misfit phase are present in our samples. For the C–E areas the content of the misfit phase is found to be 12–16 wt%, a smaller amount of BiSe (0–8 wt%), but the most dominant component is Bi_2Se_3 (around 80 wt%). The composition of part A is dominated by the misfit phase and BiSe, and only 6 wt% of Bi_2Se_3. This section is the last to crystallize during slow cooling making it Se poor and Nb rich. The phase composition of area B [with the shown PXRD pattern in Fig. 1(b)] falls between that of A and the C–E areas, with 62 wt% of Bi_2Se_3, 20 wt% of the misfit phase, and 18 wt% BiSe. Interestingly, it will be shown that S1-A is superconducting at a T_C similar to the other parts of the crystal boule ($T_{C,onset}$ for all areas of S1 are displayed in the SM [34]).

The phase composition of the other samples that will be discussed in the following sections is shown in Fig. 1(d). The main finding is that all samples investigated in this study contain the misfit layer compound, with contents ranging from 7 to 46 wt%. We also note here, that the results follow the trend of S1, e.g., S2-D is similar to S1-E, both located at the tip of the crystal boule, and S4-B is similar to S1-A positioned at the top part. An overview of the sample locations on the crystal boules can be found in the SM [34] and in Fig. 1(a). Considering the uncertainties (see the text in Fig. 1), the total integrated content of Nb in the misfit layer structure present in S1 cannot directly account for all Nb used in the synthesis, but it does suggest that most of it is contained in the misfit phase, only leaving a small fraction available for intercalation in the van der Waals gap of Bi_2Se_3.

Despite this apparently small amount of Nb available for intercalation, we investigate a possible expansion of the van der Waals gap, or rather the c axis of the Bi_2Se_3 crystal by PXRD. To this end, Fig. 2 shows a comparison of the position of the (006) reflection for the Bi_2Se_3 reference sample and powders obtained from each of the five areas of S1. By single peak fitting with a pseudo-Voigt peak profile [39], a small expansion of the c axis is detected with an average
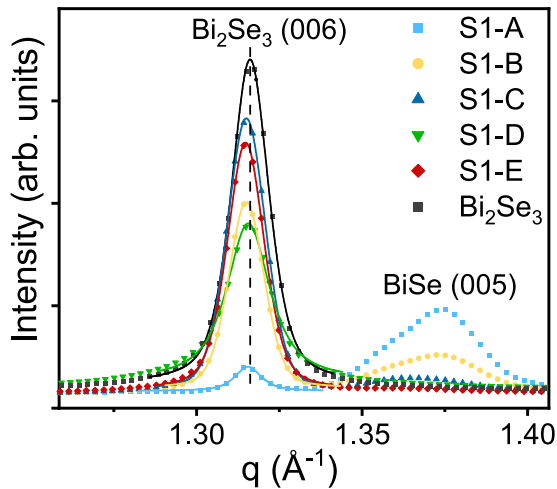
FIG. 2. High-resolution PXRD scan showing the (006) reflection from the Bi_2Se_3 structure. Presented are the five areas of the nominal $Nb_{0.25}Bi_2Se_3$ sample (S1) compared to that of a reference sample of pristine Bi_2Se_3, with data shown as points. Single peak fits with a pseudo-Voigt profile are shown as lines, with the vertical dashed line marking the (006) reflection. The (005) reflection from the BiSe structure is also visible for some of the areas (shown on the right).

FIG. 3. High-field magnetoresistance data for three nominal $Nb_{0.25}Bi_2Se_3$ samples, (a) S5-C, (b) S6-C, and (c) S7-C, at 1.3 K with the longitudinal and Hall resistance, R_{xx} and R_{xy} (green curve), for field strengths up to 30 T. R_{xx} data were measured perpendicular (black) and in plane (red curve) with respect to the sample surface. The inset in (a) shows how the contacts were mounted to the samples, with the current (I) direction indicated with respect to the applied magnetic fields $B_{\parallel}$ and $B_{\perp}$.

of 0.020 ± 0.004 Å (or 0.07%) for all sample areas in S1, but there is no trend between these values and the detected contents of misfit, BiSe, or Bi_2Se_3 phases (the method can be found described in detail together with the results in the SM [34]). Comparing this to the result in Ref. [33] with Cu-doped Bi_2Se_3, a significantly larger expansion of 0.07 Å (or 0.2%) was reported, despite Cu being a smaller atom than Nb and samples being prepared under almost same conditions. The Cu-doped Bi_2Se_3 appears to be quite different from Nb-doped, also as no evidence of any additional phase is mentioned. Later, by the electrochemical intercalation method, direct evidence of intercalation of Cu in Bi_2Se_3 was reported [40]. The expansion of the c axis has also been investigated for the Sr-doped Bi_2Se_3 system [41], and was reported to be 0.01 Å or +0.035% (no uncertainties given). These studied samples were found to contain both $SrBi_2Se_4$ (2%) and BiSe (7%) impurities, and it is unclear if this small expansion is due to intercalation.

The overall conclusions from the structural determination are as follows: All nominal $Nb_{0.25}Bi_2Se_3$ crystals investigated contain a substantial content of the misfit phase $(BiSe)_{1.1}NbSe_2$ and also some BiSe. The relative content of these phases changes over the macroscopic crystal boule, requiring a detailed determination of the actual composition for a full characterization. Indeed, the very low Nb content of the total sample available for intercalation implies that one should revisit the question of which phase gives rise to superconductivity in this material. It could be appearing due to the proximity-induced effects of a surrounding phase, similar to what is observed in the thin-film growth of $NbSe_2/Bi_2Se_3$ heterostructures [42].

It is also interesting that the cubic structure of the BiSe layers in the misfit phase could lead to the breaking of the crystals' overall threefold symmetry, possibly making the
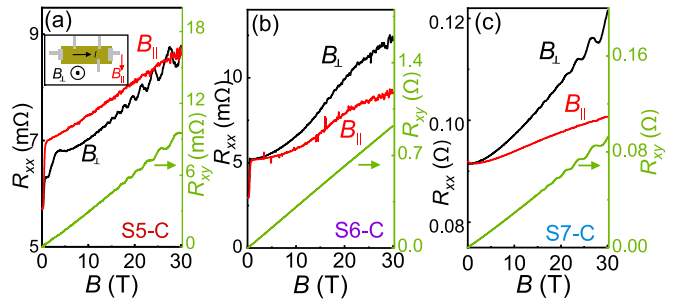
identification of nematicity in this material with spatially averaging methods challenging [22].

B. Electronic structure

The Fermi surface and charge carrier properties in the nominal $Nb_{0.25}Bi_2Se_3$ samples can be determined by measuring quantum oscillations in the resistance (Shubnikov–de Haas oscillations). In order to compare the properties of our samples to the results of previous magnetotransport experiments, e.g., Ref. [19], we have measured the high-field longitudinal and Hall resistance, R_{xx} and R_{xy}, presented in Fig. 3. The R_{xx} and R_{xy} have been measured up to 30 T at 1.3 K and were symmetrized and antisymmetrized, respectively. Measurements of R_{xx} were performed perpendicular and in plane with respect to the surface of the sample. All samples show a positive magnetoresistance. For samples S5-C and S7-C, quantum oscillations are superimposed on the magnetoresistance above 10 T if the magnetic field is applied perpendicular to the sample while they are absent in the presence of a parallel magnetic field. The observation of a sudden change in R_{xx} below 1 T is due to filamentary superconductivity and will be discussed later in this paper.

The observed Hall signal R_{xy} is linear in B and exhibits quantum oscillations for samples S5-C and S7-C. From the low-field R_{xy}, we determine the total carrier concentration n of our samples and, taking into account their thickness, and find $n_{S5-C} = 5.1 \times 10^{18}$ cm^{-3}, $n_{S6-C} = 8.8 \times 10^{19}$ cm^{-3}, and $n_{S7-C} = 2.4 \times 10^{18}$ cm^{-3}, respectively, values similar to samples studied by Lawson *et al.* of the same nominal composition [19].

We now proceed with the analysis of the quantum oscillations as a function of $B_{\perp}$. In Fig. 4, the first derivative, dR_{xx}/dB, is plotted as a function of the inverse magnetic field and the insets show the corresponding fast Fourier transforms (FFTs). For sample S7-C, we find two closely spaced frequencies at 183 and 214 T which account for the beating pattern observed in the quantum oscillations, as found also in Ref. [19] in high magnetic fields. The FFT for sample S5-C shows one dominant frequency at 206 T. Using the Onsager
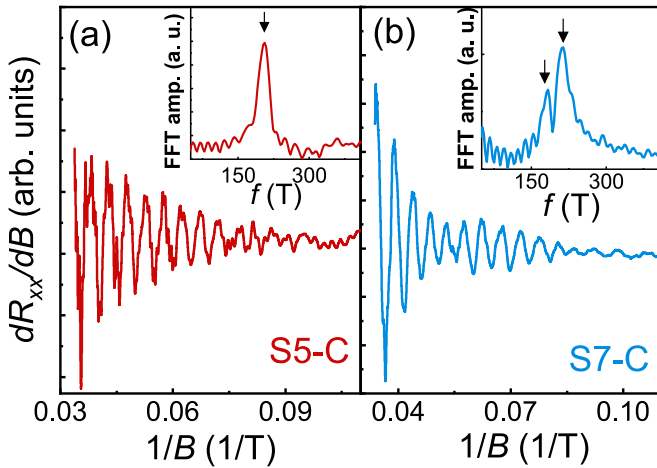
FIG. 4. High-field quantum oscillation analysis in nominal $Nb_{0.25}Bi_2Se_3$ samples at 1.3 K. The first derivative, dR_{xx}/dB, is shown as a function of $1/B$ for (a) sample S5-C and (b) sample S7-C. Insets show the corresponding fast Fourier transforms (FFTs), where arrows indicate the dominating frequencies.

FIG. 6. NanoARPES results from sample S4-B. (a) Position-dependent photoemission intensity across the sample surface, integrated in the spectral area of the yellow rectangle shown in (b). (b) Spectrum obtained by integrating the data in the spatial domain outlined by the yellow square in (a).

relation [19], these frequencies can be converted into k_F values of 0.07, 0.08, and 0.08 Å^{-1}, respectively. Values of k_F around 0.08 Å^{-1} (in the ab plane) are in good agreement with previous results [19], or with the Bi_2Se_3 in general where the carrier density extracted from the Hall resistance is generally an order of magnitude larger compared to the quantum oscillations data (see Ref. [19] and references therein).

An alternative way of electronic structure determination is to measure the band dispersion using ARPES. Figure 5 shows ARPES spectra for three nominal $Nb_{0.25}Bi_2Se_3$ samples, as well as of pure Bi_2Se_3 for comparison. The displayed (E_b, k_x) photoemission intensity spectra are extracted from a full

three-dimensional data set in which also k_y has been scanned. In this way, one can assure that the shown dispersions are taken exactly through the Brillouin zone center. The spectra contain three main features. The parabolic filled intensity at the Fermi energy around $k_x = 0$ is the bulk conduction band. The Λ-shaped intensity below ≈ 0.5 eV is the bulk valence band. In between, the Dirac cone of the topological surface state is visible, especially well for the pure Bi_2Se_3 sample. Again, a large variation between samples is observed. The topological surface state is observed quite clearly for sample S6-C; it is somewhat poorer for S4-B and very faint for S5-C. The relative doping can be judged by the binding energy of the surface state Dirac point which is somewhat higher for S4-B (≈ 410 meV) than for S6-C (≈ 350 meV). Interestingly, the Dirac point position for the nominal $Nb_{0.25}Bi_2Se_3$ sample studied in Ref. [23] was found to be 670 meV below the Fermi level and thus drastically different from the value of ≈ 400 meV found for all our samples. The data from Nb-doped Bi_2Se_3 overall resemble those from pure Bi_2Se_3 but appear to be somewhat broader and of lower quality. This could be explained by spatial averaging over slightly different structural domains. Indeed, as we shall see below, the length scale of the structural variation is smaller than the area of $\approx 190 \times 90$ μm^2 averaged over by the ARPES beam spot.

Recent experimental advances in combining ARPES with a highly focused beam of x rays have opened the possibility to observe the electronic structure of solids on a length scale below 1 μm. The results of an additional characterization of sample S4-B by this so-called nanoARPES approach are given in Fig. 6. Figure 6(a) shows a spatial photoemission intensity map across the surface of the sample. Each pixel represents the integrated intensity in an (E_b, k_x) window in the vicinity of the Bi_2Se_3 valence band, as outlined by the yellow rectangle in Fig. 6(b) which, in turn, represents the sum of all spectra taken in the yellow outlined area of Fig. 6(a). Remarkably, and in contrast to conventional ARPES, this nanoARPES spectrum shows a very well-defined surface state Dirac cone, supporting the hypothesis that the poor quality of the conventional ARPES spectra is due to the spatial averaging over many slightly different domains (for a quantitative comparison of the surface state linewidth between conventional ARPES and nanoARPES, see SM [34]). The position of the Dirac point in the nanoARPES data (binding energy of ≈ 400 meV) is similar to that derived from conventional ARPES.
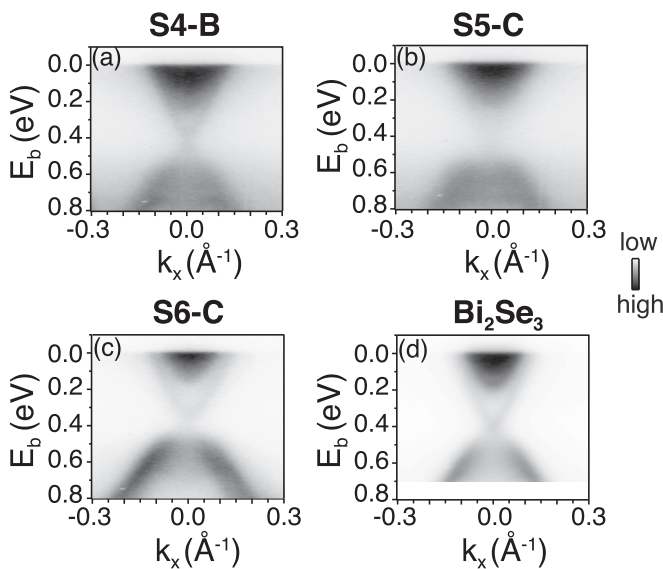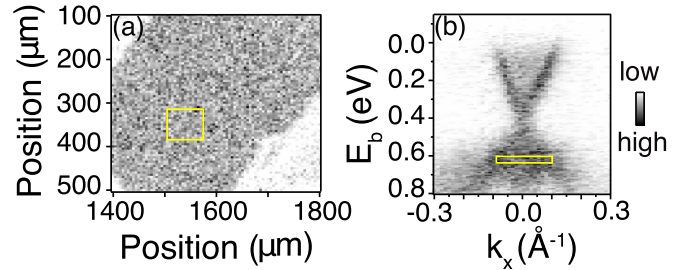

FIG. 5. ARPES photoemission intensity as a function of binding energy and k_x through the center of the Brillouin zone. Results are shown for samples S4-B, S5-C, and S6-C, as well as from a pure Bi_2Se_3 reference sample.
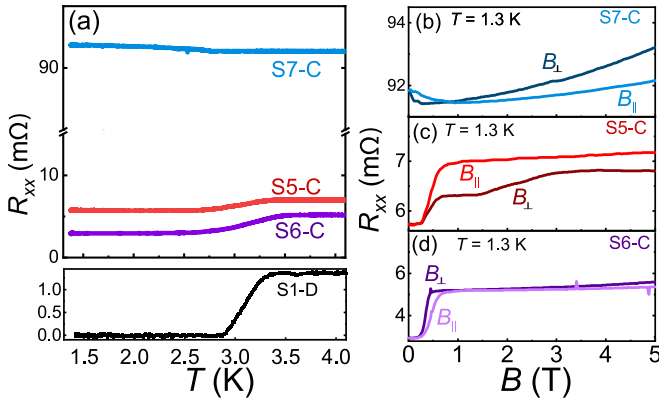
FIG. 7. (a) Zero-field resistance as function of temperature for samples S5-C, S6-C, and S7-C (and S1-D below). (b)–(d) Low-field resistance at 1.3 K both in parallel ($B_\parallel$) and perpendicular ($B_\perp$) field orientation, showing the normal and low-field resistance data for samples S5-C, S6-C, and S7-C.

The available nanoARPES data sets are dominated by regions with an electronic structure similar to that of Bi_2Se_3 rather than that of the other phases. This may be expected due to the large percentage of Bi_2Se_3 in the crystals, combined with the easy, and thus probable, cleave between quintuple layers of the Bi_2Se_3 structure.

C. Superconductivity

The superconducting properties of the samples are also subject to strong variations. Some sample areas have not been found to be superconducting, while most show T_C and $T_{C,onset}$ in the range of 2.4–3.5 K, yet they show significant variations (see SM [34]).

We first focus on the low-temperature and low-field resistance results of the samples that have been studied in the previous section. Their temperature-dependent resistance from 4.2 to 1.3 K is illustrated in Fig. 7(a). While sample S7-C shows a slight increase in R_{xx} with decreasing temperature, samples S5-C and S6-C exhibit a drop in R_{xx} below 3.5 K, that saturates below 2.5 K. A change in resistance to a nonzero value is observed for most of the samples in this study, and only a few with a $R_{xx} = 0$ drop are observed, such as for the S1-D sample in Fig. 7(a). We attribute the behavior to be due to the presence of nonconnected superconducting areas. We consider transport as a one-dimensional probe for superconductivity and assume that the drop to $R_{xx} = 0$ can be attributed to current flow in a continuous superconducting path (percolation path), as reported in Ref. [18]. In the case of, e.g., S5-C and S6-C, the current flow is incomplete, resulting in a nonzero transition.

In Figs. 7(b)–7(d), we present low-field magnetoresistance data for samples S5-C, S6-C, and S7-C for both field orientations. The magnetoresistance for sample S7-C is first negative, depending strongly on the field orientation, and then it turns positive. Samples S5-C and S6-C show the properties expected for superconductors: The resistance shows a distinct drop at a critical field, although it is not zero at the lowest temperatures. Figures 7(c) and 7(d) enable us to determine the upper critical magnetic field B_{c2}. Sample S6-C behaves
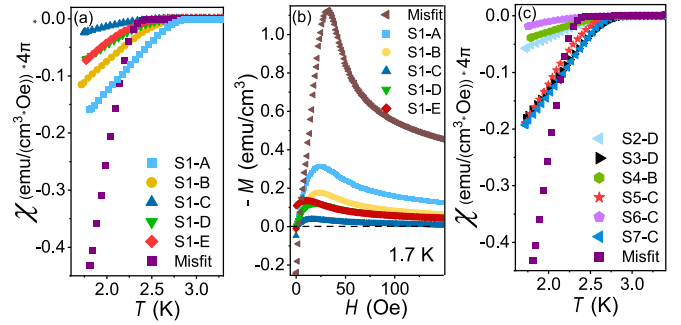

FIG. 8. (a) Volume susceptibility measured ZFC as a function of temperature with a magnetic field of 2 mT (20 Oe) for powders from all areas (A–E) of sample S1 [see Fig. 1(a)] together with volume susceptibility of the pure misfit layer compound. (b) Negative volume magnetization ($-M$) as a function of magnetic field (H) for the misfit layered sample and the S1 areas at 1.8 K. (c) Volume susceptibility measured ZFC with a magnetic field of 2 mT for powders for the S2-S7 samples investigated in this study [including ARPES (S4-S6) and magnetoresistance (S5-S7) together with the same data as in (a) for the misfit layer compound sample].

as expected with a difference in B_{c2} depending on the field orientation, but sample S5-C shows two steplike transitions as a function of $B_\perp$ but only one as a function of $B_\parallel$.

To find more detailed information on the superconducting state of the nominal $Nb_{0.25}Bi_2Se_3$ samples, we have performed ZFC temperature-dependent volume susceptibility measurements, with a magnetic field strength of 2 mT. These measurements were performed on the exact same powders as used for the PXRD measurements of all the S1 crystal boule areas (A–E), and the results are shown in Fig. 8(a). A clear transition to a superconducting shielding state is observed for all areas, but none of them reaches the perfect Meissner state of -1.

The volume susceptibility of a pure sample of the misfit layered compound is also shown in the figure. The result is consistent with the previously reported superconductivity of the $(BiSe)_{1.1}NbSe_2$ phase with a $T_{C,onset}$ of 2.4 K [43]. The onset of superconductivity in the pure misfit layer compound is lower than for the nominal $Nb_{0.25}Bi_2Se_3$ samples (for S1 the value lies in the range 2.6–2.9 K, see SM [34]). Interestingly, the misfit sample is closer to the perfect Meissner state, with a susceptibility value of -1, than any of the nominal $Nb_{0.25}Bi_2Se_3$ samples. We also note that the superconducting volume of the different areas increases with increasing misfit phase content, and that the onset of the superconducting transition in all samples lies well below the T_C of 7.2 K for pure $NbSe_2$ [44], and more close to that for monolayer $NbSe_2$ of around 3 K [45].

Among our samples, S1-A reaches the volume susceptibility closer to -1 of a perfect Meissner state [see Fig. 8(a)], but we note that none of the samples are saturated at the lowest temperature of 1.7 K. Therefore, we discuss our results here, knowing that measurements down to lower temperatures could show different results. S1-A is the area with the lowest content of Bi_2Se_3 (only 6 wt%), and the largest amount of the misfit layer compound (46 wt%) [see Fig. 1(c)]. The S1-A sample is also the one most similar to the misfit sample, as can

be seen by the behavior in the plot of the negative magnetization (M) versus magnetic field (H) for a fixed temperature of 1.7 K [see Fig. 8(b)].

The T_C's of S1-A exist at the highest temperature of the areas, with 2.9 K, not low as for the pure misfit sample (2.4 K). From the plot in Fig. 8(b) the critical fields B_{C1} are determined to be 30.44(1) Oe for the misfit sample and 25.08(2) Oe for S1-A, at which the superconductors pass into the mixed state, as for type II superconductors. This points towards the possibility that the Bi_2Se_3 has a secondary impact on superconductivity compared to the proximity effects of the present misfit layer compound. The effects increase with higher misfit phase contents, as S1-B has a T_C of 2.8 K and 20 wt% of the misfit layer compound. The lower T_C's of 2.6–2.7 K are observed for the other areas with 12–16 wt%.

The volume susceptibilities for the powders from the samples investigated from ARPES and magnetoresistance are shown in Fig. 8(c). The S4-B and S6-C samples show the smallest decrease in volume susceptibility [see Fig. 8(c)], and contain smaller amounts of Bi_2Se_3 [63–65 wt%, see Fig. 1(d)] compared to the other samples. Unexpectedly, S4-B and S6-C contain 25–30 wt% BiSe. The two samples (S4-B and S6-C) experience superconducting transitions at critical temperatures of 3.2 and 3.5 K, respectively. Neither S4-B nor S6-C show quantum oscillations [see Fig. 4(b)]. S5-C and S7-C [in Fig. 8(c)] are the samples with the largest observed drop in volume susceptibility, but also containing the largest amounts of misfit phase (11–16 wt%, compared to 7–10 wt% in S4-B and S6-C). This follows the results from the S1 areas, where S1-A had the largest decrease in volume susceptibility and the largest amount of misfit [see Fig. 1(c)]. S5-C and S7-C both show quantum oscillations in the magnetoresistant measurements [see Fig. 4(b)], but only S5-C shows a drop in resistance at 3.3 K (see SM [34]). Interestingly, only one (S3-D) out of the three samples with the largest drop in volume susceptibility (S3-D, S5-C, and S7-C) contains any BiSe, excluding this as the origin of superconductivity.

Lastly, we investigate the superconducting properties in more detail. Figure 9(a) shows resistance as a function of applied magnetic field measured at different temperatures for sample S1-D. From these measurements, the upper critical field B_{C2} can be determined [see results in Fig. 9(b)]. The coherence length ξ is then determined since for a mixed state superconductor $B_{C2} = \phi_0/(2\pi\mu_0\xi^2)$, where ϕ_0 is the flux quantum and μ_0 is the vacuum permeability [46]. The corresponding values for several crystals are plotted with dashed lines as guides to the eye in Fig. 9(b). From the inset it is seen that ξ diverges as $(1 - T/T_C)^{-1/2}$ as T_C is approached, when plotted against T/T_C [46]. A model following BCS theory with a T_C of 3.0 K is shown by the black line in the inset. It is clear that all the samples follow the trend, consistent with BCS theory for conventional superconductors, and not unconventional as reported by others [18,20–22,24,30–32].

Further investigations of the magnetic behavior were conducted on powders from the same areas as the crystals presented in Fig. 9(b). The magnetization (M) was measured as a function of magnetic field (B), from 0 to 100 mT at 2.3 K (2.5 K for S2-D) [see zoom-in in Fig. 9(c)]. B_{C1} was then determined as the point where a deviation from the linear relation between $-M$ and B appeared. From B_{C1} the London
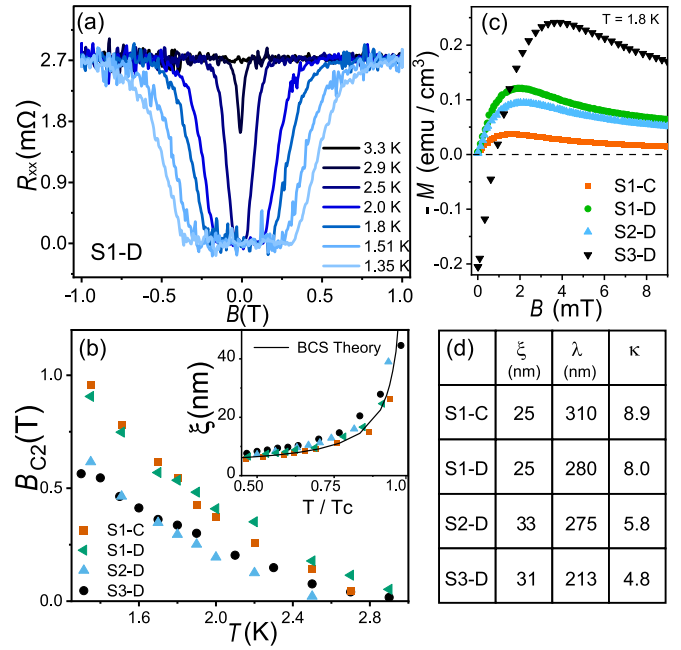

FIG. 9. (a) Resistance as a function of magnetic field for the S1-D crystal at different temperatures. (b) Upper critical field (B_{C2}) as a function of temperature for the four crystals, S1-C, S1-D, S2-D, and S3-D (error bars smaller than symbols). The inset shows the calculated coherence lengths (ξ) as a function of T/T_C for each crystal; the black line is ξ following BCS theory with a T_C of 3.0 K [46]. (c) Magnetization as a function of magnetic field for four different powder samples (S1-C, S1-D, S2-D, and S3-D), at 1.8 K (S2-D at 2.5 K). (d) Table with calculated coherence lengths (ξ), penetration depths (λ), and Ginzburg-Landau parameters (κ) for the four different samples at 2.3 K (2.5 K for S2-D). See SM for exact numbers and uncertainties [34].

penetration depth λ could be calculated from the relation $B_{C1} = \phi_0/(4\pi\mu_0\lambda^2)$ [46]. With the determined penetration depths and coherence lengths, the Ginzburg-Landau parameter $\kappa = \frac{1}{\sqrt{2}}\lambda/\xi$ for the four crystals was calculated giving $\kappa > \frac{1}{\sqrt{2}}$ in all four cases, consistent with the observed type II behavior. The obtained values of λ, ξ, and κ for the four crystals are all given in the table in Fig. 9(d). Notice that the values of λ are obtained on powders, but ξ is from crystals selected from the respective areas. The calculated λ values for the three different samples measured at 2.3 K are very similar, which also holds for ξ.

In summary, the superconducting character of the system of nominal $Nb_{0.25}Bi_2Se_3$ has a lot of similarities to that of the misfit layer compound and increased misfit content seems to be resulting in superconductivity reaching values closest to the perfect Meissner state, as the pure misfit appears to be much closer to this in Fig. 8(a), and with a volume susceptibility closer to that of the perfect Meissner state than any samples made in the $Nb_{0.25}Bi_2Se_3$ system. The results from this investigation show how the superconducting responses in the $Nb_{0.25}Bi_2Se_3$ system are of type II, and this observation is consistent with the literature [18,20]. We can, however, only speculate whether Bi_2Se_3 takes any part in the origin of bulk superconductivity. Again, we state that all Nb-doped Bi_2Se_3

samples, that have been found to be superconducting in this study, contain the misfit phase.

The results from this study on the inhomogeneous system call for a careful description of sample preparation, followed by a structural characterization when exotic phenomena are reported. The simultaneous presence of several phases is also important when discussing the details of the underlying superconducting phase. From a Nb-doped Bi_2Se_3 sample it may be possible to carefully select a smaller single crystal (as done in Ref. [19]) with high saturation and a complete drop in resistivity, but given the inhomogeneity in the system as a whole, these selected crystals should not be referred to as $Nb_{0.25}Bi_2Se_3$. An interesting issue is the observation of nodes in the superconducting gap [20,24] for which it can be important that some parts of the sample may remain metallic below T_C (ignoring the possibility of proximity-induced superconductivity) simply because of their different composition.

Recently, an increase in T_C for $(BiSe)_{1+\delta}(NbSe_2)$ was reported by Nagao *et al.* [47]. They grew single crystals and observed T_C's of 2.4 and 3.2 K for nominal compositions of $\delta = 0$ and $\delta = 0.33$, respectively. These values cover the range of the T_C's observed in this study, again suggesting the misfit phase being involved in the superconductivity in Nb-doped Bi_2Se_3, conclusions which Kamminga *et al.* [48] also recently reached in their research.

IV. CONCLUSION

The main finding of this paper is that the nominally $Nb_{0.25}Bi_2Se_3$ crystals can have a large variety of phase compositions and properties. Our results appear to challenge the widespread view of superconducting Nb-doped Bi_2Se_3 as a quasihomogeneous phase with the Nb atoms intercalated in between the van der Waals layers in the Bi_2Se_3 structure. The samples instead show contents of Bi_2Se_3, $(BiSe)_{1.1}NbSe_2$ (referred to as the misfit layer compound), and BiSe. The extreme deviation from the previous proposed composition is observed in sample S1-A [see Fig. 1(a)], with only 6 wt% Bi_2Se_3, which remains superconducting with a $T_{C,onset}$ of 2.9 K.

Only a very low Nb content of the total sample is available for any intercalation. It is rather more likely that one of the other phases is responsible for superconductivity. In the present study the pure misfit layer compound also was found to have a T_C of 2.4 K, consistent with the previously reported results [43]. Pure bulk BiSe, on the other hand, is a semiconductor [49], not found to be the origin of superconductivity. Therefore, the interplay between Bi_2Se_3 and the misfit layer compound is expected to be the reason for superconductivity, perhaps by proximity-induced effects. The results presented here are consistent with the observation of multiple Fermi surfaces in Ref. [19] because Fermi surface elements other than the Bi_2Se_3 electron pocket near the gamma point could arise in the misfit layer compound or in (slightly doped) BiSe. The relatively large contribution from the metallic misfit layer phase is of importance because it breaks the overall symmetry of the system (making it inhomogeneous and polycrystalline), such that the assumption of a threefold symmetry axis of the samples needs to be carefully evaluated when considering the possibility of symmetry breaking by nematic superconductivity [22,31].

[1] M. Z. Hasan and C. L. Kane, Rev. Mod. Phys. **82**, 3045 (2010).

[2] J. E. Moore, Nature (London) **464**, 194 (2010).

[3] Y. Ando, J. Phys. Soc. Jpn. **82**, 102001 (2013).

[4] T. O. Wehling, A. M. Black-Schaffer, and A. V. Balatsky, Adv. Phys **63**, 1 (2014).

[5] M. Sato and Y. Ando, Rep. Prog. Phys. **80**, 076501 (2017).

[6] A. Kitaev, Ann. Phys. **303**, 2 (2003).

[7] P. Zhang, K. Yaji, T. Hashimoto, Y. Ota, T. Kondo, K. Okazaki, Z. Wang, J. Wen, G. D. Gu, H. Ding *et al.*, Science **360**, 182 (2018).

[8] L. Fu and E. Berg, Phys. Rev. Lett. **105**, 097001 (2010).

[9] Y. S. Hor, A. J. Williams, J. G. Checkelsky, P. Roushan, J. Seo, Q. Xu, H. W. Zandbergen, A. Yazdani, N. P. Ong, and R. J. Cava, Phys. Rev. Lett. **104**, 057001 (2010).

[10] L. A. Wray, S.-Y. Xu, Y. Xia, Y. S. Hor, D. Qian, A. V. Fedorov, H. Lin, A. Bansil, R. J. Cava, and M. Z. Hasan, Nat. Phys. **6**, 855 (2010).

[11] S. Sasaki, M. Kriener, K. Segawa, K. Yada, Y. Tanaka, M. Sato, and Y. Ando, Phys. Rev. Lett. **107**, 217001 (2011).

[12] M. Kriener, K. Segawa, Z. Ren, S. Sasaki, S. Wada, S. Kuwabata, and Y. Ando, Phys. Rev. B **84**, 054513 (2011).

[13] J. A. Schneeloch, R. D. Zhong, Z. J. Xu, G. D. Gu, and J. M. Tranquada, Phys. Rev. B **91**, 144506 (2015).

[14] Z. Liu, X. Yao, J. Shao, M. Zuo, L. Pi, S. Tan, C. Zhang, and Y. Zhang, J. Am. Chem. Soc. **137**, 10512 (2015).

[15] Y. Pan, A. M. Nikitin, G. K. Araizi, Y. K. Huang, Y. Matsushita, T. Naka, and A. de Visser, Sci. Rep. **6**, 28632 (2016).

[16] A. Y. Kuntsevich, M. A. Bryzgalov, V. A. Prudkoglyad, V. P. Martovitskii, Y. G. Selivanov, and E. G. Chizhevskii, New J. Phys. **20**, 103022 (2018).

[17] H. Leng, D. Cherian, Y. K. Huang, J.-C. Orain, A. Amato, and A. de Visser, Phys. Rev. B **97**, 054503 (2018).

[18] Y. Qiu, K. Nocona Sanders, J. Dai, J. E. Medvedeva, W. Wu, P. Ghaemi, T. Vojta, and Y. San Hor, arXiv:1512.03519.

[19] B. J. Lawson, P. Corbae, G. Li, F. Yu, T. Asaba, C. Tinsman, Y. Qiu, J. E. Medvedeva, Y. S. Hor, and L. Li, Phys. Rev. B **94**, 041114(R) (2016).

[20] M. P. Smylie, H. Claus, U. Welp, W.-K. Kwok, Y. Qiu, Y. S. Hor, and A. Snezhko, Phys. Rev. B **94**, 180510(R) (2016).

[21] M. P. Smylie, K. Willa, H. Claus, A. Snezhko, I. Martin, W.-K. Kwok, Y. Qiu, Y. S. Hor, E. Bokari, P. Niraula *et al.*, Phys. Rev. B **96**, 115145 (2017).

[22] T. Asaba, B. J. Lawson, C. Tinsman, L. Chen, P. Corbae, G. Li, Y. Qiu, Y. S. Hor, L. Fu, and L. Li, Phys. Rev. X **7**, 011009 (2017).

[23] K. Kobayashi, T. Ueno, H. Fujiwara, T. Yokoya, and J. Akimitsu, Phys. Rev. B **95**, 180503(R) (2017).

[24] A. Sirohi, S. Das, P. Neha, K. S. Jat, S. Patnaik, and G. Sheet, Phys. Rev. B **98**, 094523 (2018).

[25] C. Kurter, A. D. K. Finck, E. D. Huemiller, J. Medvedeva, A. Weis, J. M. Atkinson, Y. Qiu, L. Shen, S. H. Lee, T. Vojta *et al.*, Nano Lett. **19**, 38 (2018).

[26] J. Wang, F. Jiao, D. Zhang, M. Chang, L. Cai, Y. Li, C. Wang, S. Tan, Q. Jing, B. Liu *et al.*, J. Phys. Chem. Solids **137**, 109208 (2020).

[27] L. Fu, Phys. Rev. B **90**, 100509(R) (2014).

[28] K. Matano, M. Kriener, K. Segawa, Y. Ando, and G.-q. Zheng, Nat. Phys. **12**, 852 (2016).

[29] S. Yonezawa, K. Tajiri, S. Nakata, Y. Nagai, Z. Wang, K. Segawa, Y. Ando, and Y. Maeno, Nat. Phys. **13**, 123 (2016).

[30] N. F. Q. Yuan, W.-Y. He, and K. T. Law, Phys. Rev. B **95**, 201109(R) (2017).

[31] J. Shen, W.-Y. He, N. F. Q. Yuan, Z. Huang, C.-w. Cho, S. H. Lee, Y. S. Hor, K. T. Law, and R. Lortz, npj Quantum Mater. **2** (2017).

[32] F. Wu and I. Martin, Phys. Rev. B **96**, 144504 (2017).

[33] Y. S. Hor, P. Roushan, H. Beidenkopf, J. Seo, D. Qu, J. G. Checkelsky, L. A. Wray, D. Hsieh, Y. Xia, S.-Y. Xu *et al.*, Phys. Rev. B **81**, 195203 (2010).

[34] See Supplemental Material at http://link.aps.org/supplemental/10.1103/PhysRevB.103.085107 for information on the synthe-sis, sample overview, structural properties, electronic structure, and superconductivity.

[35] S. V. Hoffmann, C. Søndergaard, C. Schultz, Z. Li, and P. Hofmann, Nucl. Instrum. Methods Phys. Res. A **523**, 441 (2004).

[36] M. Hoesch, T. Kim, P. Dudin, H. Wang, S. Scott, P. Harris, S. Patel, M. Matthews, D. Hawkins, S. G. Alcock *et al.*, Rev. Sci. Instrum. **88**, 013106 (2017).

[37] W. Zhou, A. Meetsma, J. de Boer, and G. Wiegers, Mater. Res. Bull. **27**, 563 (1992).

[38] D. R. Merrill, D. B. Moore, S. R. Bauers, M. Falmbigl, and D. C. Johnson, Materials **8**, 2000 (2015).

[39] F. Sánchez-Bajo and F. L. Cumbrera, J. Appl. Crystallogr. **30**, 427 (1997).

[40] J. Zhang, J. Sun, Y. Li, F. Shi, and Y. Cui, Nano Lett. **17**, 1741 (2017).

[41] Shruti, V. K. Maurya, P. Neha, P. Srivastava, and S. Patnaik, Phys. Rev. B **92**, 020506(R) (2015).

[42] W. Dai, A. Richardella, R. Du, W. Zhao, X. Liu, C. X. Liu, S.-H. Huang, R. Sankar, F. Chou, N. Samarth *et al.*, Sci. Rep. **7**, 7631 (2017).

[43] A. Nader, A. Briggs, and Y. Gotoh, Solid State Commun. **101**, 149 (1997).

[44] E. Revolinsky, G. Spiering, and D. Beerntsen, J. Phys. Chem. Solids **26**, 1029 (1965).

[45] X. Xi, Z. Wang, W. Zhao, J.-H. Park, K. T. Law, H. Berger, L. Forró, J. Shan, and K. F. Mak, Nat. Phys. **12**, 139 (2016).

[46] A. V. Narlikar, *Superconductors* (Oxford University Press, Oxford, UK, 2014).

[47] M. Nagao, A. Miura, Y. Horibe, Y. Maruyama, S. Watauchi, Y. Takano, and I. Tanaka, Solid State Commun. **321**, 114051 (2020).

[48] M. E. Kamminga, M. Batuk, J. Hadermann, and S. J. Clarke, Nat. Commun. Mater. **1**, 82 (2020).

[49] K. Majhi, K. Pal, H. Lohani, A. Banerjee, P. Mishra, A. K. Yadav, R. Ganesan, B. R. Sekhar, U. V. Waghmare, and P. S. Anil Kumar, Appl. Phys. Lett. **110**, 162102 (2017).